Science Forum (Journal of Pure and Applied Sciences)

Journal Homepage: https://atbuscienceforum.com.ng/index.php/jpas

Geomagnetic storm effects on ionospheric total electron content at Toro, Nigeria

Simon O. Ige, Samuel A. Agbana, Saeed Abioye Bello*, Kamaldeen Aduagba Yusuf

* *Department of Physics, Faculty of Physical Sciences, University of Ilorin, Kwara State, Nigeria*

ABSTRACT

Energy input into the upper atmosphere during geomagnetic storms takes the form of enhanced electric fields, currents, and energetic particle precipitation. This storm-time energy input affects the ionosphere–thermosphere coupling which leads to the balance between the storm-induced circulation and the regular circulation and determines the spatial distribution of negative and positive storm effects. This study revealed episodes of positive and negative ionospheric storm effects during these storm events with positive effects dominating the main phases at the Toro, Nigeria International Global Navigation System Satellites Service network station while the recovery period is characterized by either positive or negative effects or a combination of both. The geomagnetic storm time was determined using the geomagnetic Dst index, southward interplanetary magnetic field, and auroral electrojet index. The development of the positive ionospheric storm effect at the low latitudes is caused by the upward movement of ionization to regions of reduced recombination rate.

ARTICLE INFO

Article history:
Received 12 November 2021
Received in revised form
14 November 2021
Accepted 14 November 2021
Published 31 December 2022
Available online
31 December 2022

KEYWORDS

Total electron content
Geomagnetic storm
Ionospheric
Scintillation

1. Introduction

The ionosphere is an important region in the Earth's atmosphere useful for long-distance radio propagation and space communication systems such as global navigation system satellites (GNSS). The occurrence of ionospheric disturbances caused by geomagnetic storms affects ionospheric morphology. The physical process responsible for the ionospheric disturbances includes penetration of the electric field (Huang, 2008), disturbance dynamo zonal electric fields (Scherliess & Fejer, 1997, disturbed thermospheric winds (Pincheira et al., 2002; Richmond and Matsushita, 1975), and composition changes (Scott et al., 2014). These processes cause changes in the ionospheric measurable parameters such as the maximum electron density, maximum height of the F2 layer (Pietrella and Perrone, 2008) total electron content (TEC) (Garner et al., 2008), etc. The observable disturbed ionospheric parameters are usually irregular as they respond to the temporal and spatial perturbation caused by the intense solar event.

Trans-ionospheric radio signals from the GNSS undergo refraction and reflection from the uneven distribution of the observable ionospheric parameters. These phenomena observed from the propagation of radio signals is a function of the irregularities in the ionosphere depending on the TEC value. The TEC is driven directly by the coupling of the Sun and the Earth's ionosphere by the deposition of solar-charged particles into the ionosphere, the magnitude of which depends on the magnitude of the solar event. The

*** Corresponding author** Saeed Abioye Bello ✉ bioyesaeed@gmail.com ✉ Department of Physics, Faculty of Physical Sciences, University of Ilorin, Kwara State, Nigeria.

observed and measured TEC has been found by other researcher (e.g., Bagiya et al., 2009; Dugassa et al., 2019) to be dependent on the latitude of the receiver, the time of the day, and the season.

Extensive studies are being carried out in understanding the solar events which lead to the observable irregularities in the ionospheric parameters. These solar events include solar flares (Barta et al., 2019; Leonovich et al., 2002), solar cycle variation (Ogwala et al., 2019)ionospheric error is assumed to be somewhat of a nuisance. The error induced by the ionosphere is proportional to the number of electrons along the line of sight (LOS, coronal mass ejection (Webb and Howard, 1994), and the high-speed solar wind stream (Kirkwood et al., 2015).

The intense level of solar events is evident as a geomagnetic storm. Interaction of the particles from the solar events with the Earth's magnetosphere in the near-earth region causes field disruptions, creating electric currents. This further creates magnetic field fluctuations (Grafe and Feldstein, 2000). The ring current is formed around the Earth. The geomagnetic storm caused by the intensification of the ring current and its migration closer to the earth is characterized by depression in the horizontal component of Earth's geomagnetic field at low latitude.

During a geomagnetic storm, various energy transport takes place in the ionosphere, the energy is deposited into the ionosphere via the magnetosphere. High-latitude electric field penetrates the low, mid, and equatorial ionosphere during a geomagnetic storm leading to significant changes in the ionospheric conditions (Fejer et al., 2007; Kikuchi et al., 2003). The ionosphere's response to the geomagnetic storm, known as an ionospheric storm, manifests as a large increment or decrement in electron density profile and TEC from its ordinary level observed from global positioning system (GPS) network measurements. The increment and decrement are known as positive and negative ionospheric storms respectively (Balan et al., 2013a). Negative ionospheric storms are known to result in radio blackouts in ground-based high-frequency communication and their physical mechanisms are not well understood (Mendillo and Narvaez, 2010; Rishbeth, 1991). Positive ionospheric storms have been studied by many researchers (Balan and Rao, 1990; Basu et al., 2001; Pincheira et al., 2002). It was observed that it can lead to serious problems such as time delay, range error, and scintillation in satellite communication and navigation. Liu et al. (2010) reported the seasonal and magnetic latitude dependence of the time delays between geomagnetic disturbances and TEC response. It was also observed that there is a positive correlation between the intensity of geomagnetic disturbances and the time duration of both the positive phase and negative phase of the geomagnetic storm. The duration of both the negative phase and positive phase have clear latitudinal, seasonal, and magnetic local time dependencies.

Under disturbed conditions, ionospheric convection leads to enhanced energy and momentum dissipation in the high-latitude ionosphere and thermosphere which drives large-scale wind surges. Based on the phenomenological scenario of (Prölss (1997), these winds alter the mid-latitude ionosphere by moving plasma along field lines to regions of altered composition. On the other hand, the interconnection between southward interplanetary magnetic field (IMF) and the Earth's magnetic field leads to a strong dawn-to-dusk electric field that can have dramatic changes in the earth's ionosphere. As summarized by Tsurutani et al. (2004), these disturbance electric fields have been identified as prompt penetration zonal electric fields often observed in the equatorial latitudes (Kelley et al., 2003) and delayed electric fields produced by the disturbance dynamo driven by Joule heating due to storm energy input at high latitudes and can cause large uplifts or downdrafts of the ionospheric plasma leading to large-scale local time-dependent enhancements or decreases of the vertical TEC (VTEC) (Richmond and Lu, 2000; Scherliess and Fejer, 1997).

In this study, the seasonal effect on ionospheric TEC fluctuation during geomagnetic storms over a station at low latitudes is investigated. The TEC was analyzed in response to the dominant storm event observed across the four seasons of the year.

2. Data and Methodology

The GPS was used in the estimation of the TEC using a dual-frequency receiver to estimate the ionospheric TEC computed from the combined L1 (1,575.42 MHz) and L2 (1,227.60 MHz) pseudo ranges and the carrier phase of the GPS signal. The TEC data consist of a Receiver Independent Exchange Format file archived at the Scripps Orbits and Permanent Array Center (SOPAC) data archive (ftp://garner.ucsd.edu) which was collected by an International GNSS Service (IGS) station located at Toro (10.12°N, 9.12°E), Bauchi, Nigeria. The GPS radio signals traveling through the ionosphere are delayed by the ionospheric ionized plasma, imparting group delay to the total number of electrons encountered along the line-of-sight. When measuring TEC, the ionospheric delay and advances must be taken into account. The absolute value of the group delay, I is given as

$$I = \int \frac{X}{2} ds = \frac{80.6}{2f^2} \int N_e \, ds \tag{1}$$

Equation (1) can be written in terms of TEC as

$$I = \frac{40.3}{f^2} TEC[m] \tag{2}$$

The delay can be expressed in units of distance or time. The time delay of Equation (2) is given as

$$\Delta t = \frac{40.3}{cf^2} TEC[s] \tag{3}$$

where c is the speed of light, f, is the GPS frequency of propagating signal.

Measurement of the difference in ionospheric delays between the L1 (1,575.42 MHz) and L2 (1,227.60 MHz) GPS frequencies, which are typically considered to travel along the same path in the ionosphere. Thus, the group delay is calculated in Equation (4)

$$P_1 - P_2 = 40.3TEC\left(\frac{1}{f2^2} - \frac{1}{f1^2}\right) \tag{4}$$

P_1 and P_2 are the group path lengths corresponding to the frequencies f_1 and f_2.

By applying a simple mapping function, the slant TEC (STEC) were transformed to VTEC and assigned to an ionospheric pierce point (IPP) latitude and longitude, assuming that the ionosphere was a thin shell at 350 km in height (Huang and Yuan, 2013; Zhao and Zhou, 2019). The value of VTEC is determined from the observed STEC using the relation

$$VTEC = STEC \times \sqrt{1 - \left(\frac{R_E cos\theta}{(R_E + h_{max})}\right)^2} \tag{5}$$

where θ is the elevation of the satellite, R_E is the radius of the earth, and h_{max} the height of the ionospheric shell above the surface of the earth. The computed VTEC corresponds to the TEC at the IPP.

The data were processed with the use of the TEC retrieval software developed by Gopi Krishna Seemala of the Institute of Scientific Research, Boston College, Boston. The output of the algorithm contained the VTEC at IPP. The percentage deviation of storm time TEC (% ΔTEC) from the TEC values during the quiet periods was calculated using

$$\%\Delta TEC = \frac{TEC - TEC_m}{TEC_m} \times 100 \tag{6}$$

where TEC is the hourly observed TEC during the disturbed days and serves as the reference value which is the median value of the five quietest days in the month in which the storm occurred.

The geomagnetic parameters used include southward IMF (Bz), auroral electrojet (AE) index, geomagnetic Dst, and Kp index that were obtained from the space physics data facility accessible on https://omniweb.gsfc.nasa.gov/form/dx1.html. The days selected were based on the magnitude of the geomagnetic storm across the four seasons. The storm events analyzed are shown in Table 1 for the years 2015 and 2016.

3. Results and Discussion

3.1. 9th September 2015 storm (September equinox)

The 9th September 2015 storm event represents the September equinox. Figure 1 shows the variations of the IMF and geomagnetic parameters together with the percentage change in VTEC for a period of four days, ranging from the 7th to 10th of September. Figure 1a shows the IMF southward component (Bz) and *Dst*-index of the storm. The IMF southward component (Bz) showed a significant northward incursion at about 0000 UT on 8th September 2015 and lasted for about 9 hours peaking at 15 *nT* before changing orientation, to exhibiting a southward excursion for 6 hours. There was a sudden storm commencement (SSC) on 8th September 2015 at about 2000 UT. This

Table 1. Storm periods and classification used in the study.

Storm events	Season of storm occurrence	minimum value ()	Classification of storm
9 Sept 2015	September equinox	−98	Moderate
20,21 Dec 2015	December solstice	−155	Strong
6,7 Mar 2016	March equinox	−98	Moderate
8,9 May 2016	June solstice	−88	Moderate

The quiet days were selected based on quiet time information provided by World Data Center (WDC) Kyoto, Japan: (http://wdc-kugi.kyoto-u.ac.jp/qddays/index.html).

coincides with the IMF *Bz* turning southwards reaching a value of −2.5 *nT* 3 hours after the SSC. The *Bz* then experiences a northward movement lasting an hour before turning southwards to reach its lowest peak of −10 *nT* at 0600 UT on 9th September 2015. The commencement of the main phase of the storm coincides with the second southwards turning of the Bz after the SSC reaches its peak *Dst* minimum value of −98nT at 1200 UT on 9th September 2015. After peaking at its minimum *Dst* value, the storm enters its' recovery phase, recovering till the following day, 10th September 2015. Before the occurrence of SSC, the storm *Dst* value was relatively −8 *nT*, lasting for approximately 5 hours.

The corresponding AE index for the storm is shown in Figure 1d, at the onset of the first storm on 7th September 2015, the AE value rose to a value of 1,720 *nT*. Before the second storm, the AE index was significantly low coinciding with when the was not depressed. It then rose to a value of 1,220 *nT* during the second storm main phase. Figure 1c shows the three-hourly Kp index. At 1800 UT before the SSC, the Kp index had a value of 2. The Kp index value increased from 3.8 to 6, 9 hours after the SSC. The Kp value was reduced to 5.4 when the disturbance was at its minimum peak.

Before the 9th September storm, a storm occurred on midnight of 7th September 2015 with a minimum peak of −70 *Dst* of which its main phase began at 1300 UT lasting 7 hours to reach its minimum peak. The corresponding IMF *Bz* turned significantly northwards at 0000 UT on 8th September 2015 for 9 hours to reach its maximum peak of 15 *nT*. The 7th September storm began its recovery phase on 0200 UT on the 8th, moving to reach a *Dst* value of 0 *nT*. The *Kp* index value of the 7th September storm was considerably high with a maximum of 6.6 when the *Bz* experiences a minimum southward peak at 1500 UT during the main phase of the 7th September storm.

The percentage change in VTEC from 0600 UT on the 7th to 0600 UT on the 8th during the first storm data was not available in the data analyzed. Similarly,

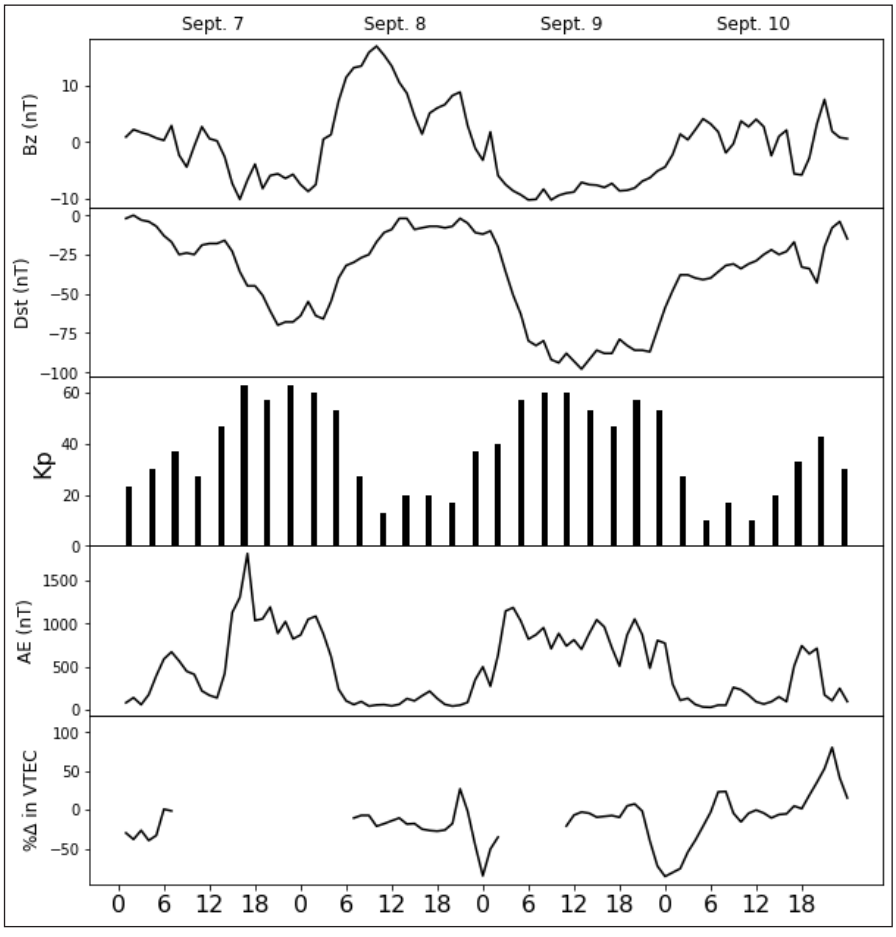

Figure 1. (a) IMF Southward (*Bz*) variation; (b) *Dst*-index variation; (c) *Kp* index; (d) AE index; and (e) % Δ VTEC for 7–10 September 2015.

for 0100 UT to 0500 UT and 0700 UT to 0900 UT on the 9th of September 2015 during storm time, no data were available. However, from the available dataset, there was a significant depletion in VTEC during the SSC at 2000 UT from +30% to −85% at 2300 UT before recovering at the onset of the storm's main phase. There was a high increase in the percentage deviation of VTEC at 0600 UT, during the storm main phase 3 hours before the storm minimum peak *Dst* with a percentage deviation value of +120%. After the peak of the storm, the VTEC experienced a quiet time for 9 hours, before it depleted considerably low with a percentage deviation value of −100%, which corresponds with the storm's recovery phase.

3.2. 20th December 2015 storm (December solstice)

This storm event represents the December solstice. Figure 2 shows the variation of the *Dst*-index, *Bz* component, AE index, Kp index, and percentage change in VTEC, respectively. From Figure 2b, the index started showing variation on the 2200 UT of 19th December 2015 which is an SSC. The storm's initial phase lasted for about 4 hours from 2300 UT to 0200 UT on the 20th of December 2015. The storm's main phase began at 0300 UT on 20th December 2015 and lasted for 19 hours. With steady descent of the index during the storm main phase, the index attained its minimum peak value of −155 *nT*, at 2100 UT on the 20th. Thereafter, it underwent recovery on 21st December, till it reaches about −30 *nT*, and continues with this value on 22nd December 2015. The corresponding IMF *Bz* component variation from Figure 2a shows that the southward component was quiet on 19th December 2015, before a northward spike at 1900 UT on the 19th, 3 hours before the SSC. At 0200 UT on the 20th, at the onset of the storm main phase, the *Bz* southward component began a significant incursion which peaks with a minimum value of approximately −19 *nT*, at 2200 UT, on 20th December 2015 at which it now starts its recovery. The IMF *Bz* component began its northward excursion right after the storm's *Dst* minimum peak.

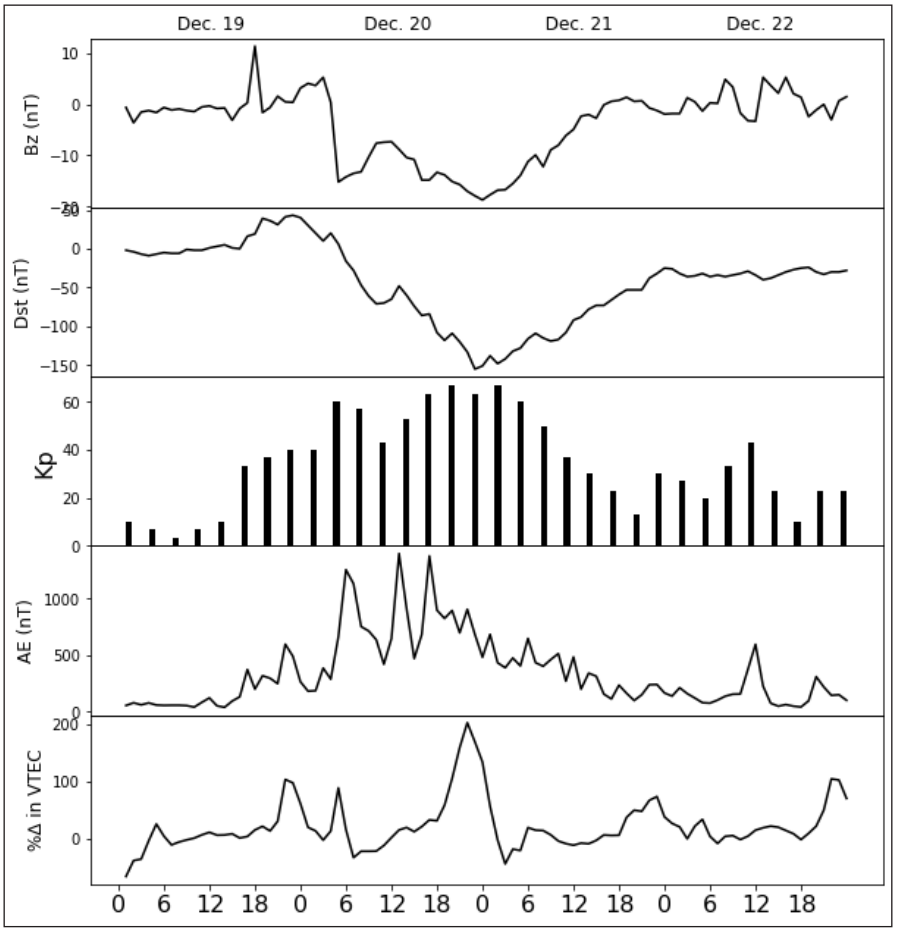

Figure 2. (a) IMF Southward (*Bz*) variation; (b) *Dst*-index variation; (c) *Kp* index; (d) AE index; and (e) % Δ VTEC for 19–22 December 2015.

Figure 2d shows the AE index which rose from 200 *nT* at 0000 UT to 1230 *nT* at 0400 UT on 20th December during the storm's initial phase. It experiences a double peak during the storm's main phase with a value of 1330 *nT*. Figure 2c shows that the Kp index has a value of 7 on 20th December 2015 at 2200 UT, the same time when the Dst index reached its minimum.

During the storms, the main phase on 20th December, the percentage change in VTEC increased to +200%, which was when the storm main phase has its minimum index. During the storm recovery phase, the VTEC got depleted.

3.3. 6th March 2016 storm (March equinox)

This storm represents the march equinox event; Figure 3 shows the geomagnetic parameter variation. From Figure 3b, the index value was quiet on 5th March 2016 before rising to about 20 *nT* at 0200 UT on 6th March 2016. For 13 hours, the Dst value was approximately steady with the value of 20 *nT*. At 1400 UT on the 6th of March, there was SSC, there was a sharp and steep descent in the value during the storm's main phase peaking at a minimum value of −98 *nT* at 2100 UT on 6th March 2016. Thereafter, it underwent recovery. The corresponding Bz variation which turned northwards on the 5th reaches its peak value of 14 *nT* at 0900 UT on the 6th, about the same time as the *Dst* index reaches its steady value. The IMF instantly turned southwards to a value of 2.5 *nT*. The IMF *Bz* turns northward to 5 nT which coincides with the onset of the SSC. After the SSC, the storm exhibits a significant southward excursion during the storm's main phase with a double peak at 1600 UT and 1900 UT with values −11 *nT* and −13 *nT* respectively. During the recovery phase of the storm, the corresponding IMF turned northwards from its minimum to settle at 0 *nT* during and after the storm's recovery phase.

From Figure 3d, the AE index rose to a value of 1210 *nT* at 1400 UT coinciding with the SSC. The corresponding Kp index value as shown in Figure 3c was significantly high with a value of 6.4 at the same time when both the *Bz* index and the IMF

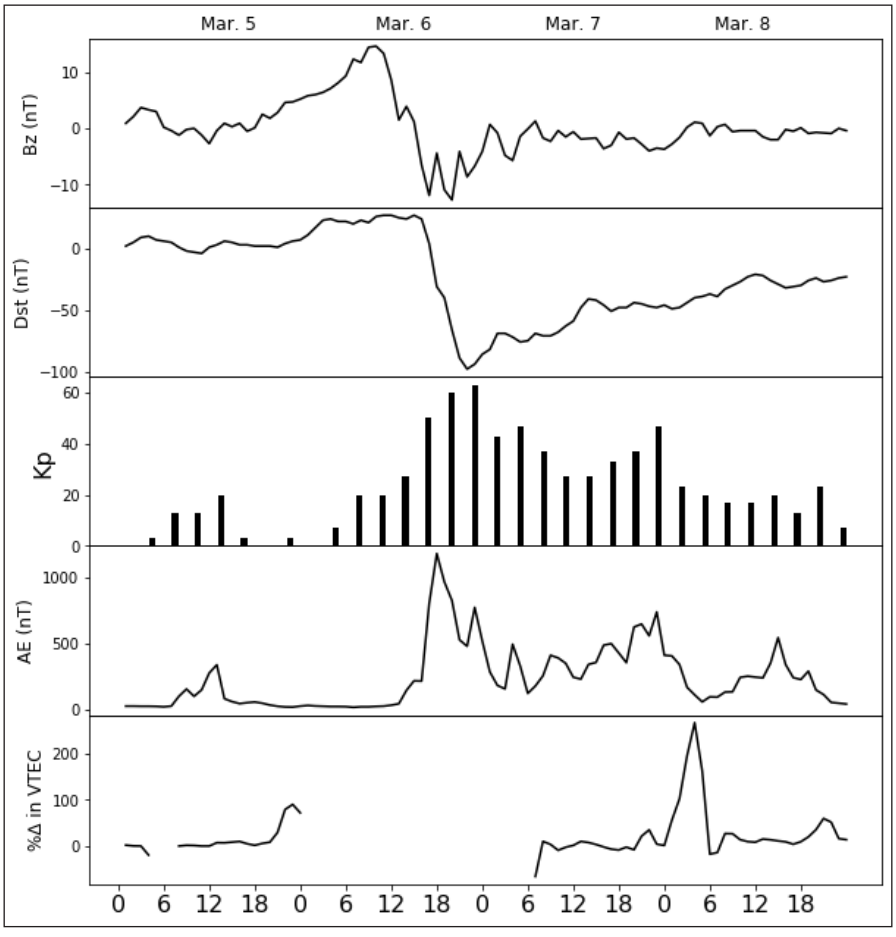

Figure 3. (a) IMF Southward (*Bz*) variation; (b) *Dst*-index variation; (c) *Kp* index; (d) AE index; and (e) % Δ VTEC for 5–8 March 2016.

component reaches their minimum. TEC data for the 6th March for which the storm occurred were not available, but there was a significant change in the VTEC, increasing to +290% right after the recovery phase of the storm before getting depleted to reach a level comparable similar to the quiet days.

3.4. 8th May 2016 storm (June solstice)

This storm represents the June solstice event. Figure 4 shows the variation of the IMF and geomagnetic parameters. Figure a and b shows the *Dst* and *Bz* of the storm. It shows that the storm was almost quiet on 7th may, 2016 with its Dst value residing at approximately −10 *nT* and it is fluctuating between −2 *nT* and 5 *nT*. The storm began its initial phase at 0100 UT on 8th May and its *Dst* underwent a fall in value on 8th May 2016. The storm main phase lasted for 5 hours from 0100 UT to 0700 UT reaching its minimum value of −88 *nT* at 0700 UT, that same day. Thereafter, it recovered for 8 hours till about −40 *nT* before it began a second SSC and fell again to peak at −80 nT. At 0000 UT on 9th May 2016, the storm's recovery phase began which lasted for 13 hours till 1300 UT on 9th May. The figure also shows the corresponding IMF *Bz* variation. On 7th May 2016, the *Bz* value was unsteady and goes high and low simultaneously. On 8th May 2016, at 0000 UT, the *Bz* turned southward at a time coinciding with the onset of the storm's initial phase.

The southward excursion of the *Bz* peaked at −12 *nT* at 0200 UT which then turned northwards to reach −5 *nT* at 0300 UT before turning southwards again to reach a peak of −11nT at 0500 UT all during the storms main phase of the storm. At the same time, the reached its peak of the first recovery phase, and the IMF Bz which had again turned northwards also peaked at −1 *nT* before alternating southward and northward twice between the values of −1 and −5 *nT* during the main phase of the second storm for 4 hours between 1500 UT and 1900 UT. When the second storm began its recovery phase, the IMF *Bz* finally turned northwards although there were miniature southward excursions. The AE index showed a significant increase in value

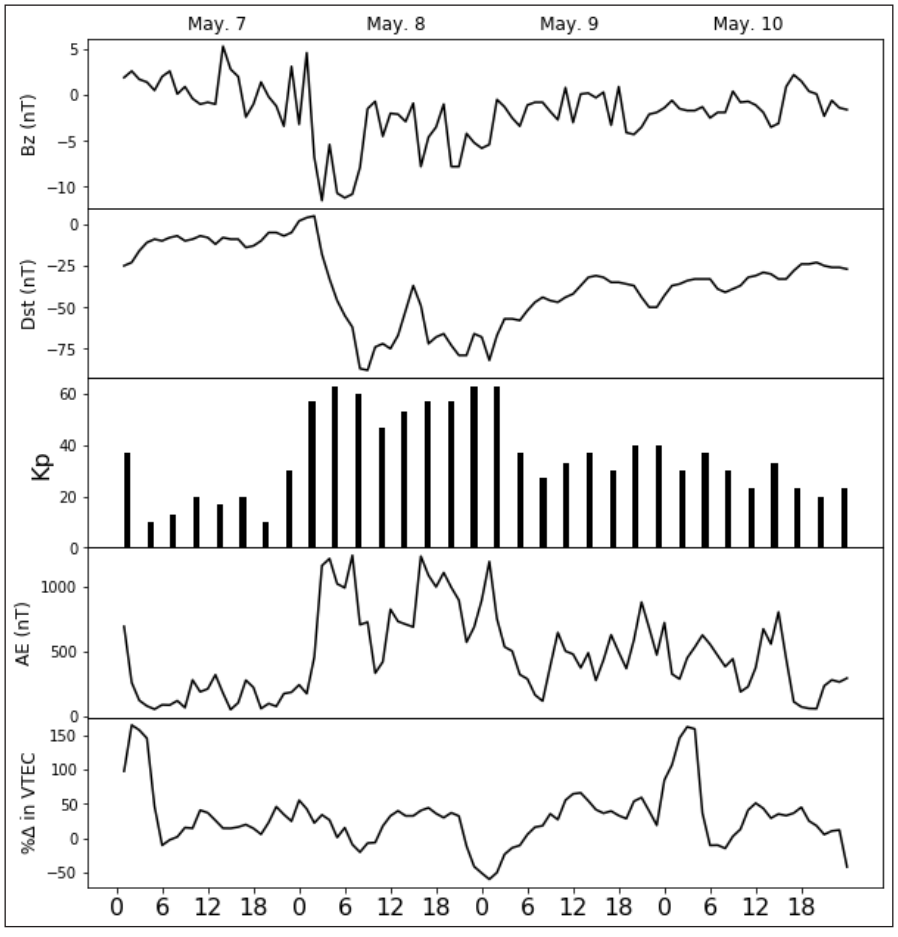

Figure 4. (a) IMF Southward (*Bz*) variation; (b) *Dst*-index variation; (c) *Kp* index; (d) AE index; and (e) % Δ VTEC for 7–10 May 2016.

at the SSC, rising to a value of 1230 nT. The AE index remained high through the storm's main phases till its final recovery at 0000 UT on the 9th.

The *Kp* index shown in Figure 4c shows that on the 7th, the value was low, because the storm was not evolving. From 0900 UT on the 7th to 0300 UT on the 8th, the *Kp* index value steadily increased which coincides with the onset of the storm's initial phase. The *Kp* index was steadily high during the course of the storm's main phase till its recovery phase.

On the 7th at 0000 UT, the percentage change in VTEC was high but underwent depletion to a quiet state at 0500 UT on the same day. During the onset of the storm's initial phase, the percentage change in VTEC was +60% and the VTEC got depleted during the storm's first main phase between 0000 UT and 0700 UT. The VTEC got replenished during its first recovery phase before undergoing its highest VTEC depletion between 1900 UT and 0000 UT on the 9th to a value of −50%. The VTEC then got replenished till 0200 UT on the 10th, to a percentage value of +180% which was its maximum immediately after the storm.

4. Discussion

Energetic particles and a stronger electric field are transferred into the upper atmosphere during geomagnetic storms (Adebiyi et al., 2015). The worldwide circulation of currents and the neutral composition of the atmosphere are disrupted as a result of this energy intake. High energy intake causes waves and changes in thermospheric winds and chemistry. As a result of geomagnetic storms, ion and electron recombination rates are affected. High-velocity disruption waves, known as traveling atmospheric disturbances (TADs) (Balthazor and Moffett, 1997), can cause the F layer to rise. As moving ionospheric disruptions, TADs manifest in the ionosphere, with increasing VTEC levels as a result. A balance between normal circulation and storm-induced circulation determines the regional distribution of positive and negative storm impacts. Storm-induced and normal circulation balance determine the spatial and temporal distribution of positive and negative storm impacts. According to investigations (Balan et al., 2013b; Zhao et al., 2012) there have been positive and negative ionospheric storms. Negative storms were few and far between during the season, in contrast to the number of positive storms. During the main period of a geomagnetic storm, a significant number of positive storms were detected.

The positive ionospheric storm is the outcome of the upward migration of ionization to regions of decreasing recombination concentrations from prior findings in the works of Lin et al. (2005) and Yuan et al. (2009). According to Zhao et al. (2009) upward plasma drift mechanisms provide mechanisms for mechanical behavior by an electric field or a storm-caused equator-neutral wind. According to Lin et al. (2005), the mechanisms of observed TEC augmentation are neutral winds caused by storms and mid-latitude Prompt Penetration Electrical fields. Prompt penetration and disruption of dynamo-electric fields are key sources of low-latitude ionospheric electrodynamic disturbances.

As the storm progresses, there is an equilibrium between a storm-induced thermospheric circulation and the daily thermosphere's composition, and the solar stage's circulation over the study point that results in a seasonal shift in TEC. In the analysis of the thermospheric composition, the ionospheric electron concentration is proportional to the atomic oxygen content (O) and the depletion is proportional to the molecular nitrogen (N_2) (Scott et al., 2014). Since the sub-solar point varies with the geomagnetic equator seasonally, it affects the TEC's storm period changes (Adebiyi et al., 2014; Trivedi et al., 2011)

In autumn and spring, when the sub-solar point is located at or close to the Equator, the sun is directly overhead the equatorial zone, resulting in increased ionization over the station. In addition, the O/N_2 the ratio is high in this area. It is a daily cycle that is synchronized with the summer hemisphere's storm-triggered circulation and background circulation (Danilov and Lastovicka, 2001). During the winter, however, neither the baseline nor the storm-induced circulations are oriented in the same direction, until night, when they reinforce each other. The O/N_2 ratio is higher in the winter than in the summer and the N_2/O disruption region will extend from the pole to lower latitudes in summer (Fang et al., 2012).

5. Conclusion

At the equatorial station at 10.12°N, 9.12°E in Toro, the seasonal difference in TEC value during storms was investigated. The TEC value was determined using data from the SOPAC data archive. The data for geomagnetic storms and quiet hours came from Kyoto and OmniWeb, respectively. September (equinox), December (solstice), March (equinox), and May (solstice) were the geomagnetic storms that were studied from 2015 to 2016. During the storm's main process, a powerful and short-lived optimistic VTEC was detected. During the storms that happened at the two equinoxes, an unequal variance of VTEC was found,

with positive and negative VTEC deviation dominating across the season.

As compared to night-time values, the results revealed that VTEC has higher values during the day. In both seasons, TEC values rise from 0600 hours LT to 1,500 hours–1700 h LT, with the highest values occurring between 1,500 hours and 1,700 hours LT. The fountain effect pattern of plasma motion from the equatorial regions around the earth's magnetic lines of force is thought to be responsible for the post-sunset increase in TEC.

Acknowledgment

The authors are grateful to the IGS data archive for providing the GPS data used for this study and also to the host station of the GPS equipment at Toro station and the Office of the Surveyor-General of the Federal Government of Nigeria. The geomagnetic data, indices, and catalog of the geomagnetic quiet days were obtained from OmniWeb and World Data Centre, Kyoto, Japan.

References

Adebiyi SJ, Adimula IA, Oladipo OA. Investigation on mid-latitude stations to storm-time variations of GPS-TEC. Adv Space Res 2015; 55(5):1339–48; doi:10.1016/j.asr.2014.11.030

Adebiyi SJ, Odeyemi OO, Adimula IA, Oladipo OA, Ikubanni SO, Adebesin BO, et al. GPS derived TEC and foF2 variability at an equatorial station and the performance of IRI-model. Adv Space Res 2014; 54(4):565–75; doi:10.1016/j.asr.2014.03.026

Bagiya MS, Joshi HP, Iyer KN, Aggarwal M, Ravindran S, Pathan BM. TEC variations during low solar activity period (2005–2007) near the equatorial ionospheric anomaly crest region in India. Annal Geophys, 2009; 27(3):1047–57.

Balan N, Otsuka Y, Nishioka M, Liu JY, Bailey GJ. Physical mechanisms of the ionospheric storms at equatorial and higher latitudes during the recovery phase of geomagnetic storms. J Geophys Res 2013a; 118(5):2660–9; doi:10.1002/jgra.50275

Balan N, Otsuka Y, Nishioka M, Liu JY, Bailey GJ. Physical mechanisms of the ionospheric storms at equatorial and higher latitudes during the recovery phase of geomagnetic storms. J Geophys Res 2013b; 118(5):2660–69.

Balan N, Rao PB. Dependence of ionospheric response on the local time of sudden commencement and the intensity of geomagnetic storms. J Atmosph Terrest Phys 1990; 52(4):269–75.

Balthazor RL, Moffett RJ. A study of atmospheric gravity waves and travelling ionospheric disturbances at equatorial latitudes. Annal Geophys 1997; 15(8):1048; doi: 10.1007/s005850050523

Barta V, Sátori G, Berényi KA, Kis Á, Williams E. Effects of solar flares on the ionosphere as shown by the dynamics of ionograms recorded in Europe and South Africa. Annal Geophys 2019; 37(4):747–61.

Basu S, Basu S, Groves KM, Yeh HC, Su SY, Rich FJ, et al. Response of the equatorial ionosphere in the South Atlantic region to the great magnetic storm of July 15, 2000. Geophys Res Lett 2001; 28(18):3577–80.

Danilov AD, Lastovicka J. Effects of geomagnetic storms on the ionosphere and atmosphere. Int J Geomagnet Aeronom, 2001; 2(3):209–24.

Dugassa T, Bosco Habarulema J, Nigussie M. Investigation of the relationship between the spatial gradient of total electron content (TEC) between two nearby stations and the occurrence of ionospheric irregularities. Annal Geophys, 2019; 37(6):1161–80; doi:10.5194/angeo-37-1161-2019

Fang H, Weng L, Sheng Z. Variations in the thermosphere and ionosphere response to the 17–20 April 2002 geomagnetic storms. Adv Space Res 2012; 49(10):1529–36.

Fejer BG, Jensen JW, Kikuchi T, Abdu MA, Chau JL. Equatorial ionospheric electric fields during the November 2004 magnetic storm. J Geophys Res 2007; 112(A10) :1–11.

Garner TW, Gaussiran Ii TL, Tolman BW, Harris RB, Calfas RS, Gallagher H. Total electron content measurements in ionospheric physics. Adv Space Res 2008; 42(4):720–6.

Grafe A, Feldstein YI. About the relationship between auroral electrojets and ring currents. Annal Geophys 2000; 18(8):874–86; doi:10.1007/s00585-000-0874-4

Huang C. Continuous penetration of the interplanetary electric field to the equatorial ionosphere over eight hours during intense geomagnetic storms. J Geophys Res 2008; 113(A11) :1–10.

Huang Z, Yuan H. Analysis and improvement of ionospheric thin shell model used in SBAS for China region. Adv Space Res 2013; 51(11):2035–42; doi:10.1016/j.asr.2012.12.018

Kelley MC, Makela JJ, Chau JL, Nicolls MJ. Penetration of the solar wind electric field into the magnetosphere/ionosphere system. Geophys Res Lett 2003; 30(4) :1–4.

Kikuchi T, Hashimoto KK, Kitamura TI, Tachihara H, Fejer B. Equatorial counter electrojets during substorms. J Geophys Res 2003; 108(A11) :1–13.

Kirkwood S, Osepian A, Belova E, Lee YS. High-speed solar wind streams and polar mesosphere winter echoes at Troll, Antarctica. Annal Geophys 2015; 33(6):609–22.

Leonovich LA, Afraimovich EL, Romanova EB, Taschilin AV. Estimating the contribution from different ionospheric regions to the TEC response to the solar flares using data from the international GPS network. Annal Geophys 2002; 20(12):1935–41.

Lin CH, Richmond AD, Heelis RA, Bailey GJ, Lu G, Liu JY, et al. Theoretical study of the low-and midlatitude ionospheric electron density enhancement during the October 2003 superstorm: Relative importance of the neutral wind and the electric field. J Geophys Res 2005; 110(A12) :1–14.

Liu J, Zhao B, Liu L. Time delay and duration of ionospheric total electron content responses to geomagnetic disturbances. Annal Geophys 2010; 28(3):795–805.

Mendillo M, Narvaez C. Ionospheric storms at geophysically-equivalent sites–Part 2: Local time storm patterns for sub-auroral ionospheres. Annal Geophys 2010; 28(7):1449–62.

Ogwala A, Somoye EO, Ogunmodimu O, Adeniji-Adele RA, Onori EO, Oyedokun O. Diurnal, seasonal and solar cycle variation in total electron content and comparison with IRI-2016 model at Birnin Kebbi. Annal Geophys 2019; 37(5):775–89; doi:10.5194/angeo-37-775-2019

Pietrella M, Perrone L. A local ionospheric model for forecasting the critical frequency of the F2 layer during disturbed geomagnetic and ionospheric conditions. Annal Geophys 2008; 26(2):323–34.

Pincheira XT, Abdu MA, Batista IS, Richards PG. An investigation of ionospheric responses, and disturbance thermospheric winds, during magnetic storms over South American sector. J Geophys Res 2002; 107(A11):SIA–12.

Prölss GW. Magnetic storm associated perturbations of the upper atmosphere. Mag Storm 1997; 98:227–41.

Richmond AD, Lu G. Upper-atmospheric effects of magnetic storms: a brief tutorial. J Atmos Sol Terr Phys 2000; 62(12):1115–27.

Richmond AD, Matsushita S. Thermospheric response to a magnetic substorm. J Geophys Res 1975; 80(19):2839–50.

Rishbeth H. F-region storms and thermospheric dynamics. J Geomagnet Geoelectr 1991; 43(Supplement1):513–24.

Scherliess L, Fejer BG. Storm time dependence of equatorial disturbance dynamo zonal electric fields. J Geophys Res 1997; 102(A11):24037–46.

Scott CJ, Stamper R, Rishbeth H. Long-term changes in thermospheric composition inferred from a spectral analysis of ionospheric F-region data. Annal Geophys 2014; 32(2):113–9.

Trivedi R, Jain A, Jain S, Gwal AK. Study of TEC changes during geomagnetic storms occurred near the crest of the equatorial ionospheric ionization anomaly in the Indian sector. Adv Space Res 2011; 48(10):1617–30.

Tsurutani B, Mannucci A, Iijima B, Ali Abdu M, Sobral JH. A, Gonzalez W, Guarnieri F, Tsuda T, Saito A, Yumoto K, Fejer B, Fuller-Rowell TJ, Kozyra J, Foster JC, Coster A & Vasyliunas VM. J Geophys Res 2004; 109:A08302.

Webb DF, Howard RA. The solar cycle variation of coronal mass ejections and the solar wind mass flux. J GeophysRes 1994; 99(A3):4201–20.

Yuan Z, Ning B, Deng X. Effects of TADs on the F region of the mid-latitude ionosphere during an intense geomagnetic storm. Adv Space Res 2009; 44(9):1013–8.

Zhao B, Wan W, Lei J, Wei Y, Sahai Y, Reinisch B. Positive ionospheric storm effects at Latin America longitude during the superstorm of 20–22 November 2003: Revisit. Annal Geophys 2012; 30(5):831–40.

Zhao J, Zhou C. Validation and application of optimal ionospheric shell height model for single-site estimation of total electron content. Annal Geophys 2019; 37(2):263–71; doi:10.5194/angeo-37-263-2019